

Accreting Neutron Stars and their Magnetic Properties

Madeline Clyburn¹, Andrew Melatos², and Ryan Brunet²

¹*Department of Physics and Astronomy, Clemson University, Clemson, South Carolina 29634 USA*

²*School of Physics, University of Melbourne, Parkville, VIC, 3010. Australia.*

(Dated: October 16, 2021)

Previous studies on the magnetically confined mountains located at the polar caps of accreting neutron stars in x-ray binary systems have analytically guessed the mass distribution of the accreted plasma. The research discussed in this paper aims to determine the extent with which the mass-flux functional form affects the magnetohydrodynamic properties of the star after accretion. The functional form of the mass-flux was altered systematically three times and the plots of the magnetic field, ψ contours, and density were studied relative to previous results in the isothermal atmosphere limit [1]. Noticeable affects in the form of the final magnetic field and density structure suggests a dependence on the functional form of $dM/d\psi$. Additionally, the ellipticity differs significantly for each altered form, which is important in the context of the detection of gravitational waves from neutron stars with polar cap mountains. Future work in this research is needed to determine the source of numerical errors observed and interesting cases including the effects on the magnetic fields below the Neutron star surface.

I. INTRODUCTION

A potential candidate for continuous gravitational wave sources and one of the main targets with ground-based detection sites such as LIGO are neutron stars in x-ray binaries [2]. An x-ray binary consists of a neutron star with a companion white-dwarf or super-giant star. Not only are these stars spinning rapidly with periods in the millisecond range, but also as time evolves, the neutron star accretes material from its' companion star via stellar winds or by disc accretion. The accreted material from the companion star flows along the magnetic field lines of the neutron star and accumulates in a column to form a “mountain” at the polar caps which is predicted to produce disturbances in space-time if the polar axis is off-axis to the spin axis [1].

Additionally, neutron stars vary in a wide range of magnetic field strengths: from 10^7 G up to 10^{15} G [3]. The observed spin-down rate of the star due to magnetic dipole radiation allows the determination of these external magnetic field values. Previous studies on binary systems containing a neutron star, show a significant decay and evolution in the magnetic fields of these stellar bodies [4]. A hypothesis to the cause of magnetic field evolution on the surface of the neutron stars in x-ray binaries is magnetic burial. As more and more accreted plasma increases the size of the polar cap mountain, the mountain eventually buckles due to the pressure at the base. When $M_a \approx 10^{-5} M_\odot$, the hydrostatic pressure gradient exceeds the magnetic tension, and the base of the mountain spreads laterally towards the equator, dragging frozen-in magnetic flux along with it as seen in Figure 1 [5]. Ultimately, this changes the magnetic field along the surface of the star and significantly decreases the magnetic field strength.

The mass-flux of the accreted material is modeled using the Grad-Shafranov methods. The calculations in this paper are performed under the assumption of infinite conductivity or no resistivity and hence flux freez-

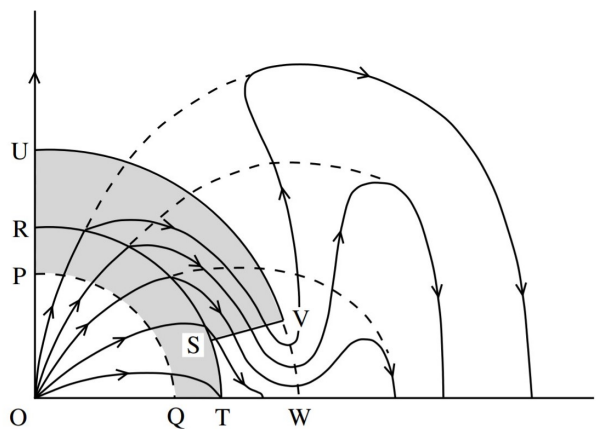


FIG. 1: Schematic diagram of the magnetic field of a neutron star (cross section) during polar cap accretion [5].

ing [1]. Previous research has not constrained the mass-flux distribution relative to the initial state until *Payne & Melatos (2004)*. They assumed a self-consistent approach whereby the arbitrary $F(\psi)$ function is calculated explicitly by imposing that the mass-flux distribution of the final state equals that of the initial state, plus the accreted material [1]. Additionally, they state, “we have checked that the solution of the Grad-Shafranov equation and $F(\psi)$ is not sensitive to the exact functional form of $dM/d\psi$, the mass-flux.” This statement begs to question, to what extent do the solutions to the Grad-Shafranov equation variate with different mass-flux functions? This paper seeks to determine alternate self-consistent mass-flux distributions to model the magnetic burial on neutron stars and to find the extent to which the solutions rely on the form of $dM/d\psi$.

Section II defines the Grad-Shafranov derivation and the methods used by the code to model the mountain on the neutron star. In section III the reproduction of results from [1] can be found with explanations to dif-

ferences in results. Altered mass-flux functions and their analysis is detailed in sections IV - VI. We then analyze these results in section VII. Section VIII describes the ellipticity results and significance to the mass-flux functional form. Finally, in section IX we summarize the results and provide areas for improvement and future work.

II. THEORY

The only forces acting on the plasma accreted by a neutron star in an x-ray binary are the Lorentz force from the magnetic field of the neutron star,

$$\vec{F}_B = q(\vec{v} \times \vec{B}), \quad (1)$$

where q is the charge, \vec{v} is the velocity, and \vec{B} is the magnetic field, the pressure gradient force per volume ∇p , and the gravitational force $m\vec{g}$, with mass m and gravitational field of the neutron star g . Using Newton's Second Law,

$$\vec{F} = m\vec{a}, \quad (2)$$

we can write

$$\frac{\vec{F}}{V} = \frac{q}{V}(\vec{v} \times \vec{B}) - \nabla p + \rho\vec{g} = \rho \frac{d\vec{v}}{dt}. \quad (3)$$

Equation 3 can be rewritten with the vector potential $\vec{g} = -\nabla\Phi$, and the diamagnetic current $\vec{J} = \sigma\vec{v}$ and $\sigma = q/V$, where σ is the volume charge density, and V is the volume:

$$\rho\vec{a} = \vec{J} \times \vec{B} - \nabla p - \rho\nabla\Phi. \quad (4)$$

Using Maxwell's Equation at the magnetostatic limit

$$\nabla \times \vec{B} = \mu_0 \vec{J}, \quad (5)$$

we can write in the more conventional notation

$$\rho \frac{d\vec{v}}{dt} + \rho(\vec{v} \cdot \nabla)\vec{v} = \frac{1}{\mu_0}(\nabla \times \vec{B}) \times \vec{B} - \nabla p - \rho\nabla\Phi. \quad (6)$$

In the magnetostatic limit we can rewrite Equation 6 where $\vec{v} = 0$ and $\partial/\partial t = 0$,

$$\nabla p + \rho\nabla\Phi - \frac{1}{\mu_0}(\nabla \times \vec{B}) \times \vec{B} = 0. \quad (7)$$

Next we can use another one of Maxwell's equations ($\nabla \cdot \vec{B} = 0$) to rewrite \vec{B} in terms of a vector potential \vec{A} .

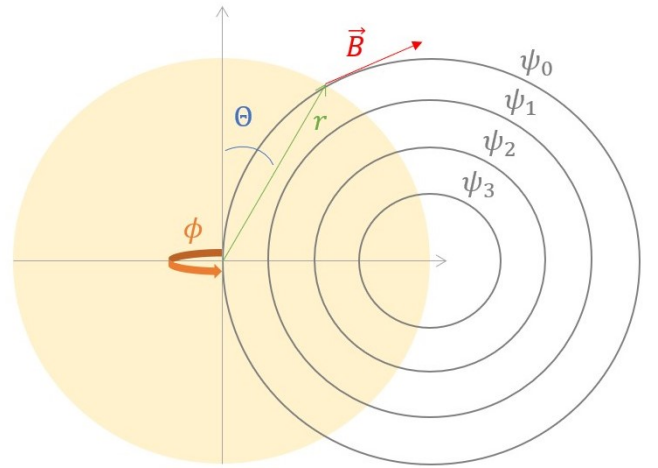


FIG. 2: Neutron star (in yellow) with dipolar magnetic field lines tangent to constant poloidal flux lines and spherical coordinate system geometry: r, θ, ϕ .

Considering a spherical geometry as in Figure 2 that is axisymmetric such that $B_\phi = 0$, we can derive the poloidal components of the \vec{B} field.

$$\begin{aligned} \vec{B} &= \nabla \times \vec{A} \\ &= \frac{1}{r \sin \theta} \left[\frac{\partial}{\partial \theta} (\sin \theta A_\phi) - \frac{\partial A_\theta}{\partial \phi} \right] \hat{r} \\ &\quad + \frac{1}{r} \left[\frac{1}{\sin \theta} \frac{\partial A_r}{\partial \phi} - \frac{\partial}{\partial r} (r A_\phi) \right] \hat{\theta} \\ &\quad + \frac{1}{r} \left[\frac{\partial}{\partial r} (r A_\theta) - \frac{\partial A_r}{\partial \theta} \right] \hat{\phi} \\ &= \frac{1}{r \sin \theta} \frac{\partial}{\partial \theta} (\sin \theta A_\phi) \hat{r} - \frac{1}{r} \frac{\partial}{\partial r} (r A_\phi) \hat{\theta} + B_\phi \hat{\phi} \\ &= \frac{1}{r^2 \sin \theta} \frac{\partial}{\partial \theta} (r \sin \theta A_\phi) \hat{r} - \frac{1}{r \sin \theta} \frac{\partial}{\partial r} (r \sin \theta A_\phi) \hat{\theta} \end{aligned}$$

Since r and θ are independent from one another, the remaining \hat{r} and $\hat{\theta}$ components make up the poloidal field B_p . We can then create a new term known as the poloidal flux $\psi = r \sin \theta A_\phi$. Therefore we can write the poloidal magnetic field in terms of this poloidal flux,

$$\vec{B}_p = \frac{1}{r \sin \theta} \nabla \psi \times \hat{\phi}. \quad (8)$$

Next, using the remaining Maxwell's Equation in Equation 5

$$\begin{aligned}
\nabla \times \vec{B} &= \nabla \times \left(\frac{1}{r \sin \theta} \nabla \psi \times \hat{\phi} \right) \\
&= \frac{1}{r \sin \theta} \nabla \psi \left(\nabla \cdot \hat{\phi} \right) - \hat{\phi} \left(\nabla \cdot \frac{1}{r \sin \theta} \nabla \psi \right) \\
&\quad + \left(\hat{\phi} \cdot \nabla \right) \frac{1}{r \sin \theta} \nabla \psi - \left(\frac{1}{r \sin \theta} \nabla \psi \cdot \nabla \right) \hat{\phi} \\
&= -\hat{\phi} \left(\nabla \cdot \frac{1}{r \sin \theta} \nabla \psi \right) \\
&= \mu_0 \vec{J}
\end{aligned}$$

Notice that this is just the toroidal current J_ϕ . Finally, we can work out the final component of Equation 7

$$\begin{aligned}
(\nabla \times \vec{B}) \times \vec{B} &= \left(-\hat{\phi} \left(\nabla \cdot \frac{1}{r \sin \theta} \nabla \psi \right) \right) \\
&\quad \times \left(\frac{1}{r \sin \theta} \nabla \psi \times \hat{\phi} \right) \\
&= -\frac{1}{r \sin \theta} \left(\nabla \cdot \frac{1}{r \sin \theta} \nabla \psi \right) \left[\nabla \psi \left(\hat{\phi} \cdot \hat{\phi} \right) \right. \\
&\quad \left. - \hat{\phi} \left(\hat{\phi} \cdot \nabla \psi \right) \right] \\
&= -\frac{1}{r \sin \theta} \left(\nabla \cdot \frac{1}{r \sin \theta} \nabla \psi \right) \nabla \psi
\end{aligned}$$

We can then combine all of these results to rewrite Equation 7

$$\begin{aligned}
\nabla p + \rho \nabla \Phi + \frac{1}{\mu_0 r \sin \theta} \left(\nabla \cdot \frac{1}{r \sin \theta} \nabla \psi \right) \nabla \psi &= 0 \quad (9) \\
\nabla p + \rho \nabla \Phi + (\Delta^2 \psi) \nabla \psi &= 0,
\end{aligned}$$

where

$$\Delta^2 = \frac{1}{\mu_0 r^2 \sin^2 \theta} \left[\frac{\partial^2}{\partial r^2} + \frac{\sin \theta}{r^2} \frac{\partial}{\partial \theta} \left(\frac{1}{\sin \theta} \frac{\partial}{\partial \theta} \right) \right]. \quad (10)$$

Assuming an isothermal atmosphere such that $p = c_s^2 \rho$, where c_s is the isothermal sound speed. We can then use the method of characteristics to solve Equation 9. First, we rewrote Equation 9 in terms of r and θ components:

$$\begin{aligned}
c_s^2 \frac{\partial \rho}{\partial r} + \rho \frac{\partial \Phi}{\partial r} + (\Delta^2 \psi) \frac{\partial \psi}{\partial r} &= 0 \\
\rho_r + \frac{\Delta^2 \psi}{c_s^2} \psi_r &= -\frac{\rho \Phi_r}{c_s^2},
\end{aligned} \quad (11)$$

and

$$\begin{aligned}
c_s^2 \frac{\partial \rho}{\partial \theta} + \rho \frac{\partial \Phi}{\partial \theta} + (\Delta^2 \psi) \frac{\partial \psi}{\partial \theta} &= 0 \\
c_s^2 \rho_\theta + (\Delta^2 \psi) \psi_\theta &= 0,
\end{aligned} \quad (12)$$

where subscripts imply derivatives. Next we solved for $\Delta^2 \psi$ for each Equation 11 and 12

$$\begin{aligned}
\Delta^2 \psi &= -\frac{\rho \Phi_r - \rho_r c_s^2}{\psi_r} \\
&= -\frac{\rho_\theta c_s^2}{\psi_\theta}
\end{aligned}$$

$$\Rightarrow \rho_r - \frac{\psi_r}{\psi_\theta} \rho_\theta = -\frac{\rho \Phi_r}{c_s^2}$$

Given a partial differential equation of the form $a(r, \theta, \rho) \frac{\partial \rho}{\partial r} + b(r, \theta, \rho) \frac{\partial \rho}{\partial \theta} = c(r, \theta, \rho)$ we have a characteristic such that

$$\frac{dr}{a(r, \theta, \rho)} = \frac{d\theta}{b(r, \theta, \rho)} = \frac{d\rho}{c(r, \theta, \rho)} \quad (13)$$

Thus, using the result above we can write

$$\frac{dr}{1} = -\frac{\psi_\theta d\theta}{\psi_r} = -\frac{c_s^2 d\rho}{\rho \Phi_r}. \quad (14)$$

This allows us to find two more equations:

$$\psi_r dr + \psi_\theta d\theta = 0 \quad (15)$$

and

$$\Phi_r dr = -c_s^2 \frac{1}{\rho} d\rho. \quad (16)$$

Integrating both sides of Equations 15 and 16 yields

$$\psi = C_1 \quad (17)$$

and

$$\Phi = -c_s^2 \ln(\rho) + C_2. \quad (18)$$

Choosing a general function $f(\psi) = \ln(\rho) + \Phi/c_s^2$ we can solve for pressure as a function of ψ

$$\begin{aligned} \rho &= e^{f(\psi)} - e^{-\Phi/c_s^2} \\ &= F(\psi)e^{-(\Phi-\Phi_0)/c_s^2} \\ \Rightarrow p &= \frac{F(\psi)}{c_s^2} e^{-(\Phi-\Phi_0)/c_s^2}, \end{aligned} \quad (19)$$

where $\Phi_0 = GM_*/R_*$ is a reference potential and $F(\psi) = e^{f(\psi)}$ is an arbitrary function. We also know that ∇F is parallel to $\nabla\psi$ or $\nabla F = F'(\psi)\nabla\psi$. Therefore, Equation 9 can be rewritten

$$\Delta^2\psi = -F'(\psi)e^{-(\Phi-\Phi_0)}, \quad (20)$$

to form the second order, nonlinear partial differential equation. In the past, many guessed the form of $F(\psi)$. Alternatively, Payne and Melatos [1] utilized a self-consistent approach to derive $F(\psi)$ assuming that the mass-flux of the final state equals that of the initial state added to the accreted material. The amount of mass dM confined between the flux surfaces ψ and $\psi+d\psi$ is

$$\frac{dM}{d\psi} = 2\pi \int_C ds \rho[r(s), \theta(s)] r \sin\theta |\nabla\psi|^{-1}. \quad (21)$$

We can then substitute Equation 19 into Equation 21 to obtain a self-consistent expression for the arbitrary function $F(\psi)$

$$F(\psi) = \frac{c_s^2}{2\pi} \frac{dM}{d\psi} \left(\int_C ds r \sin\theta |\nabla\psi|^{-1} e^{-(\Phi-\Phi_0)/c_s^2} \right)^{-1}, \quad (22)$$

which can be solved along with Equation 20 to find $\psi(r, \theta)$ given a mass-flux ratio.

III. REPRODUCTION OF PREVIOUS RESULTS

Using the isothermal atmosphere limit as explained above, we reproduce the results of the hydro-magnetic structure of the ‘mountain’ formed by the accreted material at the poles found in [1]. We utilized the 2D Grad-Shafranov code from [6] in C/C++ with initial conditions: neutron star initial mass $M_* = 1.4 M_\odot$, neutron star radius $R_* = 10^4$ m, initial magnetic field strength $B_* = 10^8$ T, speed of sound in the isothermal crust model $c_s = 10^6$ m/s, accreted mass $M_a = 10^{-5} M_\odot$, ψ_*/ψ_a factor $b = 3$, and Iterations = 200. Using the default and arbitrarily defined mass function as in [1]

$$M(\psi) = \frac{M_a(1 - e^{-\psi/\psi_a})}{2(1 - e^{-\psi_*/\psi_a})}, \quad (23)$$

where M_a is the accreted mass, ψ is the poloidal flux contours, ψ_* is the flux surface at the stellar equator, and ψ_a is the flux surface at R_a , the radius of the accretion disk. Notice that although we describe this mass distribution as ‘‘arbitrary,’’ the form of the mass function is constrained to monotonically increase as well as ‘‘pile’’ up the material primarily at the poles. Otherwise, the exact reason for formulation of this Equation 23 is arbitrary. A plot of the default mass distribution per contour can be found in Figure ???. Differentiating Equation 23 with respect to ψ yields the mass-flux used in [1]

$$\frac{dM}{d\psi} = \frac{M_a}{2(1 - e^{-\psi_*/\psi_a})} \left(\frac{1}{\psi_a} e^{-\psi/\psi_a} \right), \quad (24)$$

with normalization variables M_0 and ψ_0

$$\frac{dM}{d\psi} = \frac{M_a}{2M_0(1 - e^{-\psi_*/\psi_a})} \left(\frac{\psi_0}{\psi_a} e^{-\psi\psi_0/\psi_a} \right). \quad (25)$$

A plot of the mass-flux ratio as a function of ψ can be found in Figure 3 which is just the derivative of Equation 23.

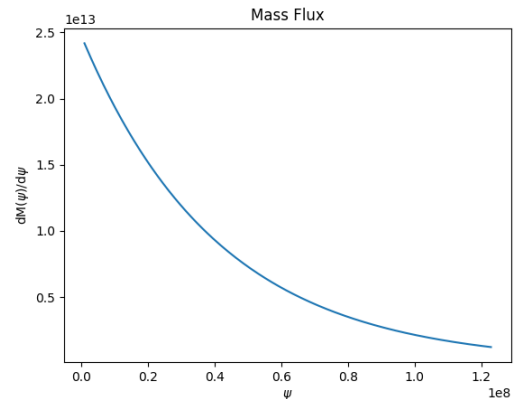


FIG. 3: Plot of Eqn. 25 where both axis are scaled to be unitless.

Below in Figure 4 are (r, θ) contour plots scaled logarithmically where appropriate to emphasize the boundary layer of compressed magnetic fields. The color scale ranges from yellow, for maximum values, to purple, for minimum values of the parameter plotted. These plots were used to qualitatively check whether our results aligned with the results in [1] with the same initial conditions as listed above. The appendix contains the original plots from the *Payne & Melatos 2004* publication for comparison.

The plots in Figure 4 clearly demonstrate the distorted magnetic field or ‘‘equatorial tuft’’ as predicted by previous research [5]. The plots of B , ρ , J , $J \times B$, and ∇p clearly resemble the same forms as in [1] besides some numerical issues mentioned below.

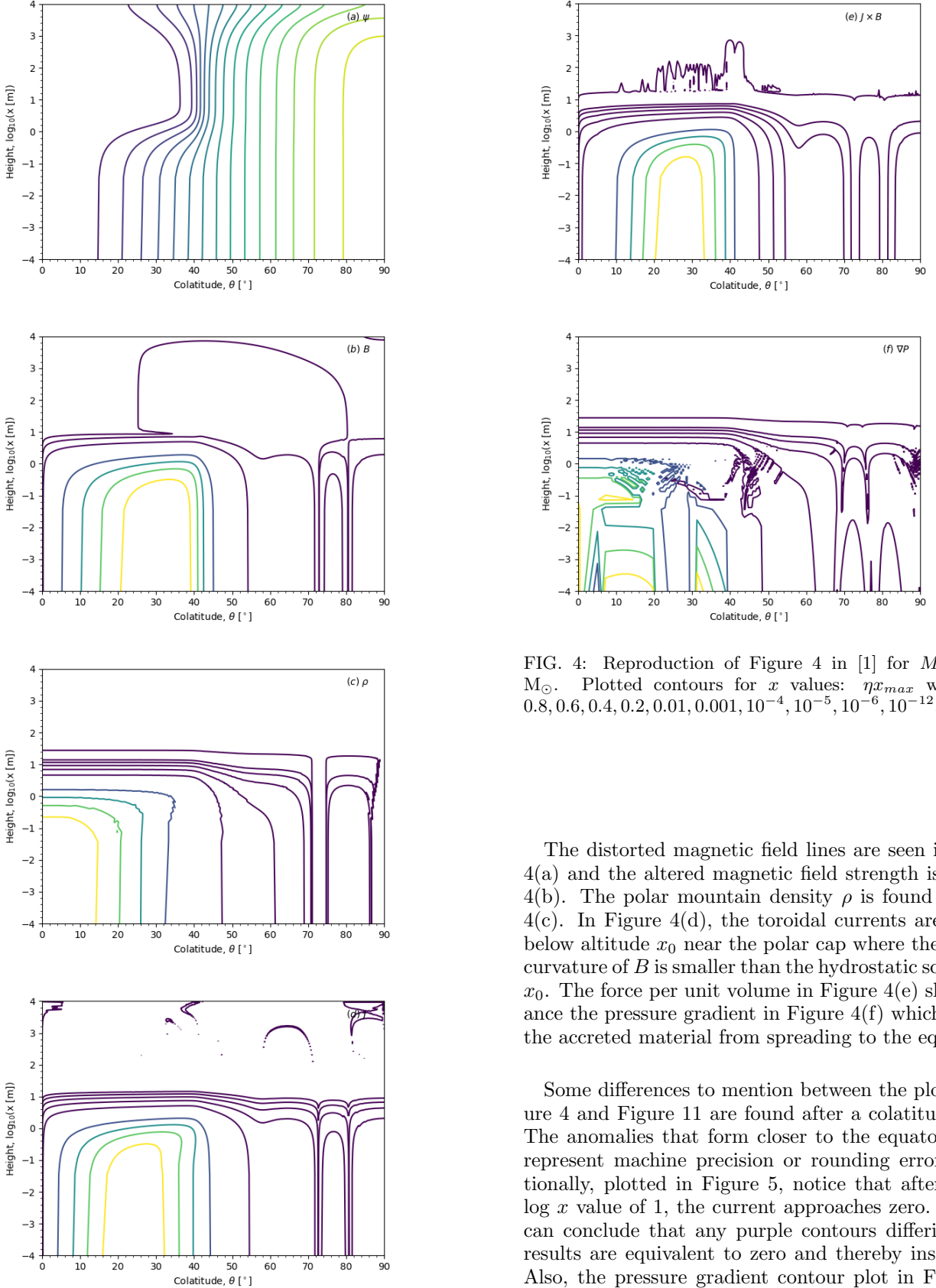


FIG. 4: Reproduction of Figure 4 in [1] for $M_a = 10^{-5} M_{\odot}$. Plotted contours for x values: ηx_{max} where $\eta = 0.8, 0.6, 0.4, 0.2, 0.01, 0.001, 10^{-4}, 10^{-5}, 10^{-6}, 10^{-12}$.

The distorted magnetic field lines are seen in Figures 4(a) and the altered magnetic field strength is found in 4(b). The polar mountain density ρ is found in Figure 4(c). In Figure 4(d), the toroidal currents are confined below altitude x_0 near the polar cap where the radius of curvature of B is smaller than the hydrostatic scale height x_0 . The force per unit volume in Figure 4(e) should balance the pressure gradient in Figure 4(f) which prevents the accreted material from spreading to the equator.

Some differences to mention between the plots in Figure 4 and Figure 11 are found after a colatitude of 70° . The anomalies that form closer to the equator seem to represent machine precision or rounding errors. Additionally, plotted in Figure 5, notice that after a scaled log x value of 1, the current approaches zero. Thus, we can conclude that any purple contours differing in our results are equivalent to zero and thereby insignificant. Also, the pressure gradient contour plot in Figure 4(f) shows signs of numerical instabilities that have not been resolved at this point.

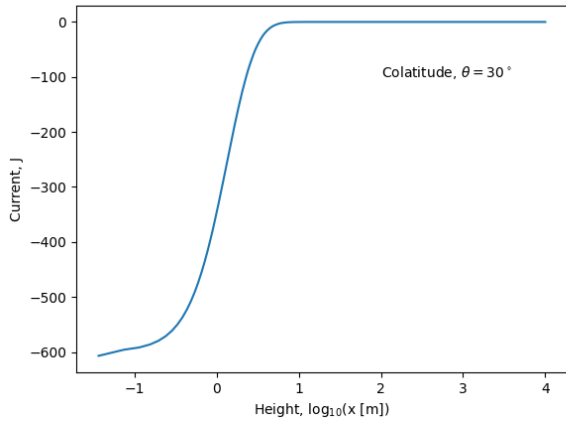


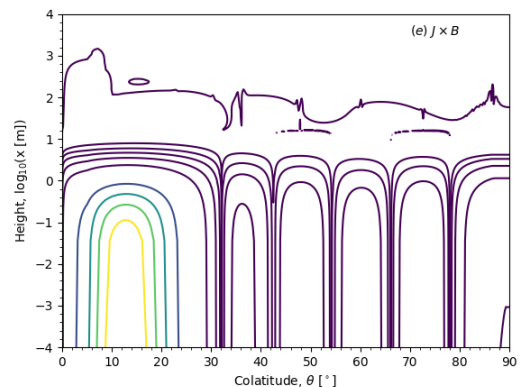
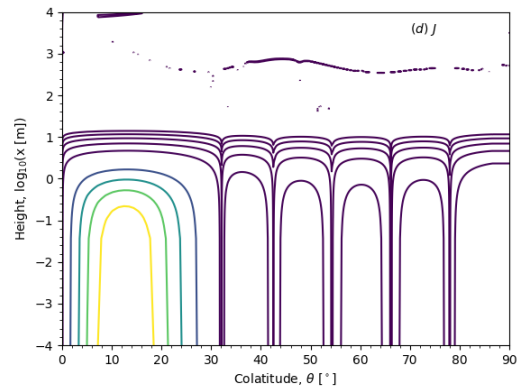
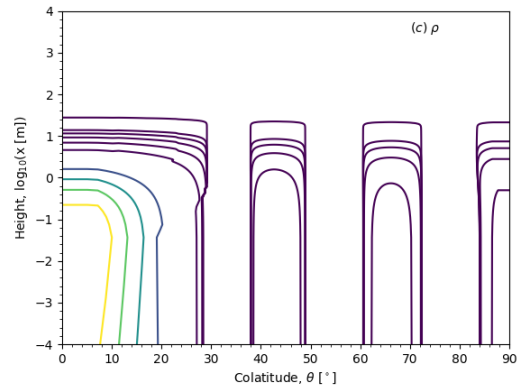
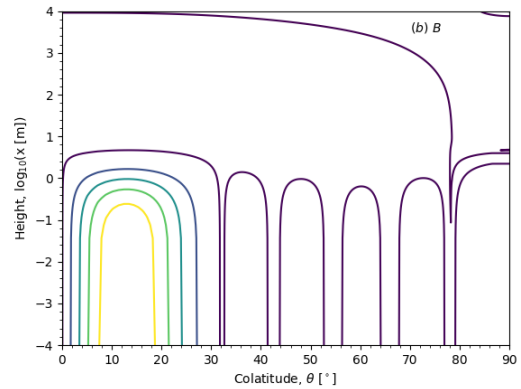
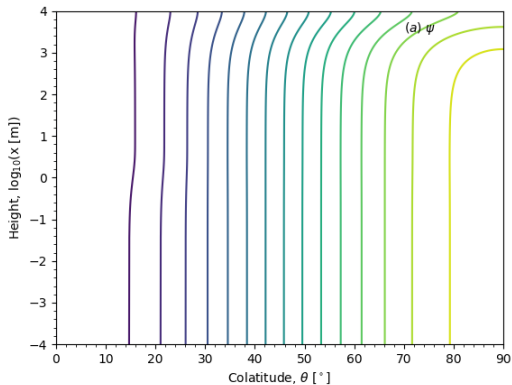
FIG. 5: Plot of current vs. logarithmically scaled height at a constant colatitude of 30° .

IV. ALTERED MASS-FLUX #1

We can modify Equation 25 to have a modified, but not drastically different form as the first altered mass-flux ratio. In this first case, the only difference between the original and first altered mass-flux is the squared ψ term in the exponential:

$$\frac{dM}{d\psi} = \frac{M_a}{2M_0(1 - e^{-\psi/\psi_a})} \left(\frac{\psi_0}{\psi_a} e^{-(\psi\psi_0/\psi_a)^2} \right), \quad (26)$$

and notice the effects on Figure 4 as seen below.



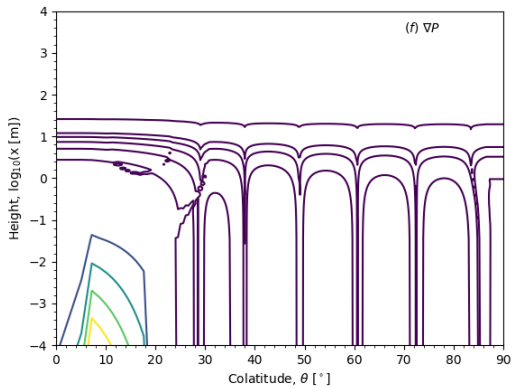


FIG. 6: Contour plots with Equation 24 for $M_a = 10^{-7} M_\odot$. Plotted contours for x values: ηx_{max} where $\eta = 0.8, 0.6, 0.4, 0.2, 0.01, 0.001, 10^{-4}, 10^{-5}, 10^{-6}, 10^{-12}$.

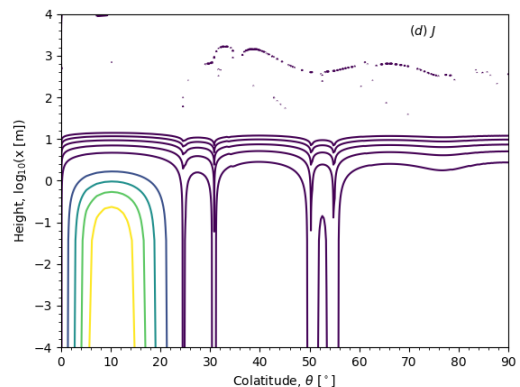
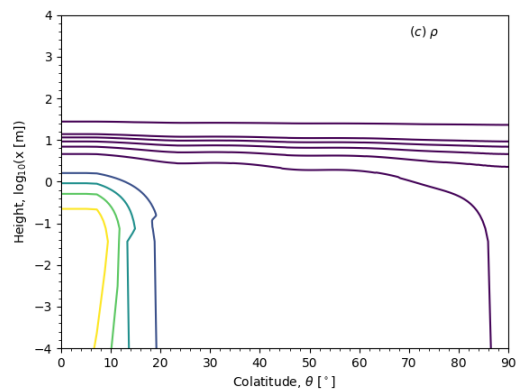
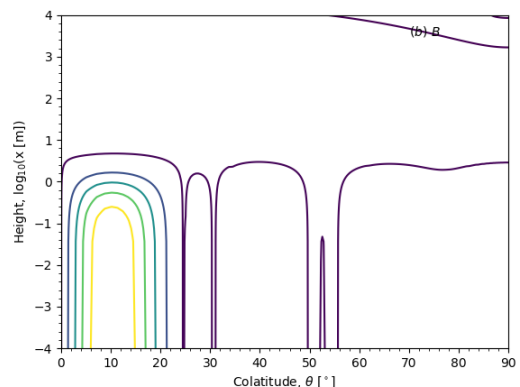
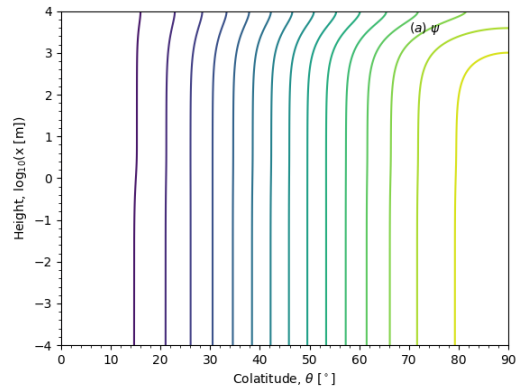
Additionally, the accreted mass magnitude for the three altered mass-flux forms was decreased by a couple magnitudes ($M_a = 10^{-7}$) due to the numerical instabilities that form from the initial condition which set in for $M_a > M_c$. Currently, we do not know M_c for the altered $dM/d\psi$ used and thus, this provides slightly weaker effects but with less numerical error.

V. ALTERED MASS-FLUX #2

The second altered mass-flux ratio was altered without an exponential but with a power to the negative 1/2. This just signifies an inverse relationship between the ψ contour and the amount of mass accreted at that ψ contour. Therefore, as ψ increases we get further from the pole and less mass is accreted at these locations. This agrees with the theory as the plasma should be affected more by the strong magnetic field lines closer to the pole to the form the so called “mountain.” Equation 25 modified to have this different form:

$$\frac{dM}{d\psi} = \frac{M_a}{2M_0} \left((\psi + \kappa) \frac{\psi_0}{\psi_a} \right)^{-1/2}, \quad (27)$$

where $\kappa = 100$ is a constant to reduce division by zero errors and notice the effects on Figure 4.



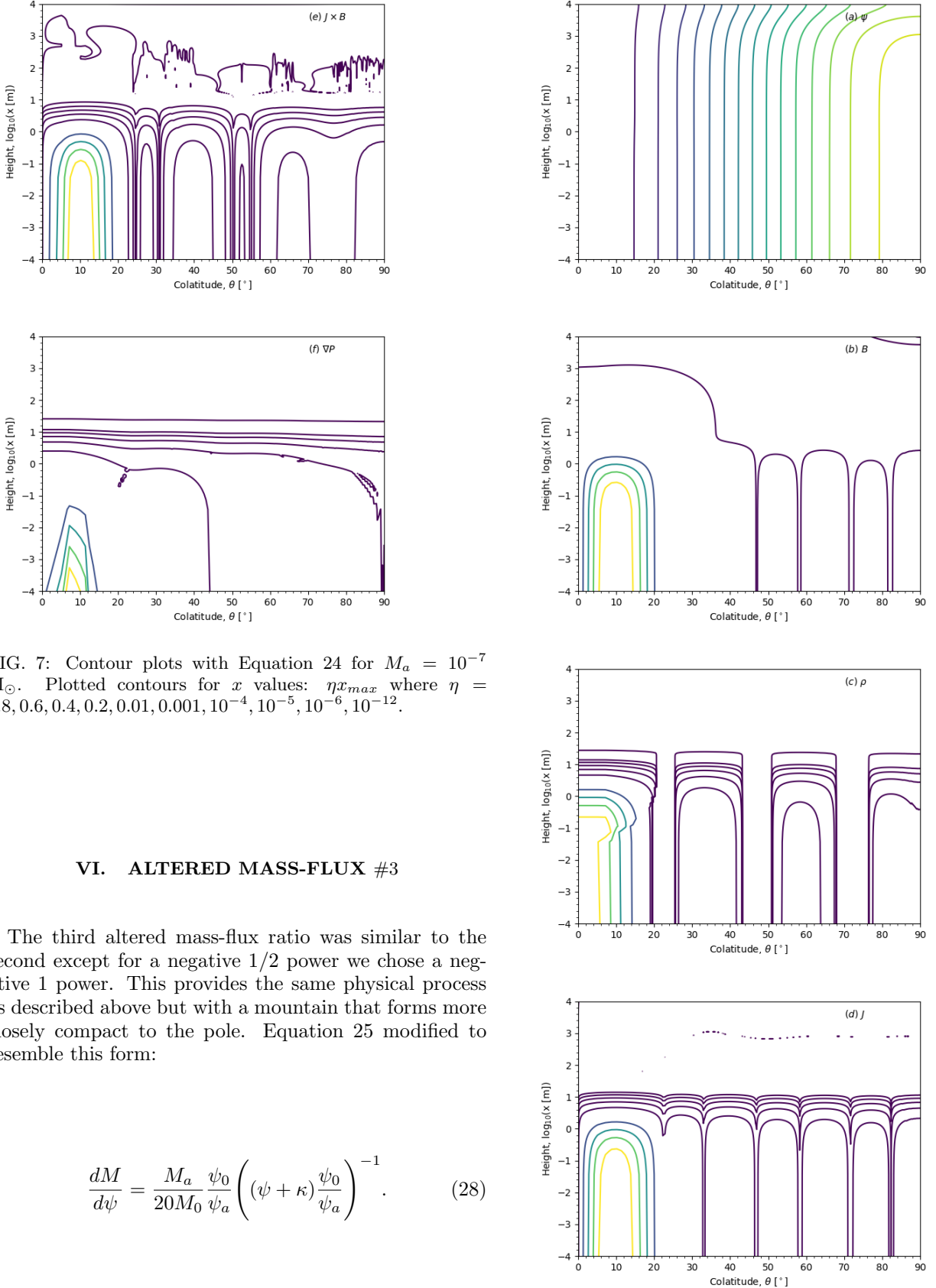


FIG. 7: Contour plots with Equation 24 for $M_a = 10^{-7} M_\odot$. Plotted contours for x values: ηx_{max} where $\eta = 0.8, 0.6, 0.4, 0.2, 0.01, 0.001, 10^{-4}, 10^{-5}, 10^{-6}, 10^{-12}$.

VI. ALTERED MASS-FLUX #3

The third altered mass-flux ratio was similar to the second except for a negative 1/2 power we chose a negative 1 power. This provides the same physical process as described above but with a mountain that forms more closely compact to the pole. Equation 25 modified to resemble this form:

$$\frac{dM}{d\psi} = \frac{M_a}{20M_0} \frac{\psi_0}{\psi_a} \left((\psi + \kappa) \frac{\psi_0}{\psi_a} \right)^{-1}. \quad (28)$$

where $\kappa = 100$ is a constant to reduce division by zero errors and notice the effects on Figure 4.

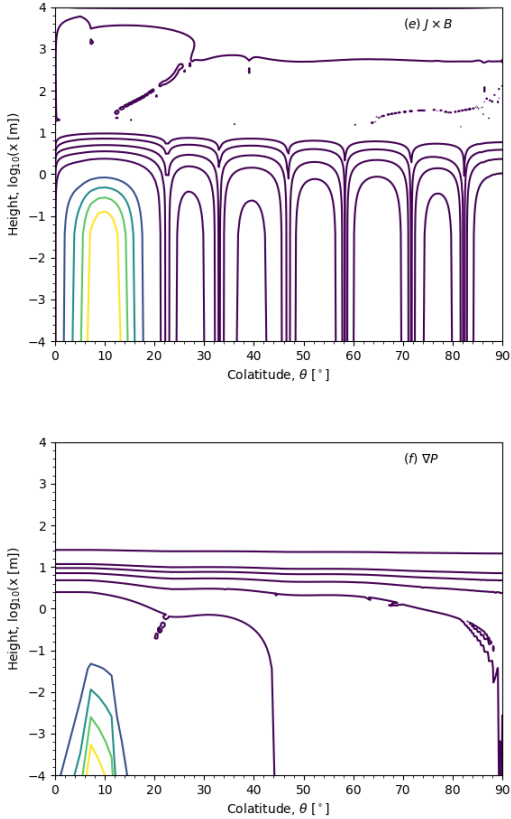


FIG. 8: Contour plots with Equation 24 for $M_a = 10^{-7} M_\odot$. Plotted contours for x values: ηx_{max} where $\eta = 0.8, 0.6, 0.4, 0.2, 0.01, 0.001, 10^{-4}, 10^{-5}, 10^{-6}, 10^{-12}$.

VII. ANALYSIS

A comparison between the original 'default' mass-flux ratio used in [1] and the three altered $dM/d\psi$ can be found in Figure 9. The physical forms of the mass-flux were not altered significantly such that the mass distribution was monotonically increasing and the mountain was constrained to build up at the poles as predicted in theory. Notice, that the altered mass-flux's #2 and #3 are unbounded at the poles and thus imply infinite mass at the poles which is mitigated by the added constant κ .

Notice that the ψ contours in Figures 6(a), 7(a), and 8(a) are not as deformed as in Figure 4. This could be mainly due to the fact that we decreased the value of the accreted mass constant by two degrees of magnitude. The effects of magnetic burial might not be as evident at this value of accreted material, however, results in the other contour plots show evidence of changes.

The major differences between the contour plots for different mass-flux function forms lie in the plots of B , ρ , and ∇P . For the magnetic field strength plots in Figures 6(b), 7(b), and 8(b), the maximum field strength (yellow contours) is shifted from a colatitude of approximately 30° to a colatitude of 10° . Additionally, the density plots

in Figures 6(c), 7(c), and 8(c) have mountains forming at the pole (same location) but with more density closer to the poles. This seems to imply smaller mountains or more dense mountains forming. Finally, the pressure gradient contour plots in Figures 6(f), 7(f), and 8(f) differ significantly from the plot in Figure 4(f) that has drastic numerical errors. This also might be due to the decreased M_a value, but also could imply that different functional forms of $dM/d\psi$ change the form of ∇P .

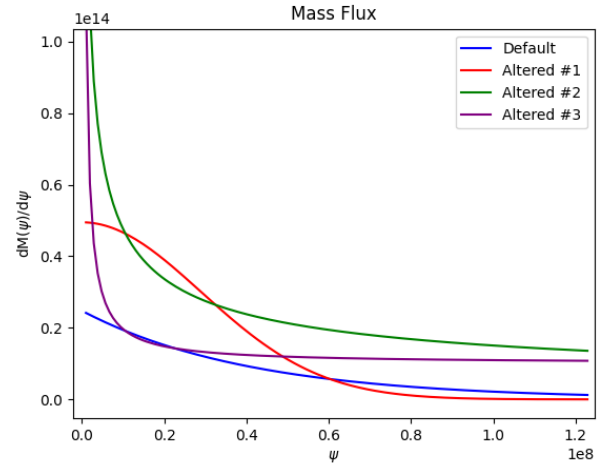


FIG. 9: Comparison of mass-flux ratio forms.

VIII. ELLIPTICITY

As material is accreted on the neutron star's polar caps and mountains form, the star becomes more elliptic. The ellipticity is a value used to describe the degree of deviation from a sphere. In general, the ellipticity of a spinning neutron star accreting mass can be used for the detection of gravitational waves. The ellipticity is directly proportional to the amplitude of the gravitational wave and thus an important parameter to numerically determine for detection. The ellipticity, ϵ can be calculated with

$$\epsilon = \frac{|I_{zz} - I_{yy}|}{I_0}, \quad (29)$$

where $I_0 = 2/5 M_* R_*^2$ and I_{jk} is the moment of inertia tensor such that the z -axis lies along the magnetic axis of symmetry [6]. We can write using the moment of inertia tensor definition:

$$I_{zz} = \int (x^2 + y^2) dM, \quad (30)$$

and

$$I_{yy} = \int (x^2 + z^2) dM. \quad (31)$$

Using Equation 29, the Priymak code evaluates the ellipticity at each point within the iterative process. In Figure 10, one can find the ellipticity values for each mass-flux distribution with varying accreted mass values. Current work is being done to determine the accuracy of these predictions for the altered mass-flux distributions, however these results bring hope to continuous gravitational wave searches. According to the most recent search for gravitational waves from isolated neutron stars, the minimum ellipticity of the star must be $\epsilon = 4 \times 10^{-7}$ at a distance of 6 kpc and high frequency spin [7]. Our results not only align with these results from LIGO as in most of the ellipticity values lie in the range given, but also the varying values for ellipticity depending on the mass-flux functional form suggests that the mass-flux distribution is critical to understanding the gravitational waves emitted from neutron stars with magnetically confined mountains.

FIG. 10: Ellipticity ϵ for the different mass flux distributions and varying accreted mass values.

$dM/d\psi$	M_a/M_\odot	ϵ
$\frac{M_a}{2M_0(1-e^{-\psi_*/\psi_a})} \left(\frac{\psi_0}{\psi_a} e^{-\psi\psi_0/\psi_a} \right)$	10^{-9}	1.50×10^{-9}
	10^{-7}	1.72×10^{-7}
	10^{-5}	1.33×10^{-5}
$\frac{M_a}{2M_0(1-e^{-\psi_*/\psi_a})} \left(\frac{\psi_0}{\psi_a} e^{-(\psi\psi_0/\psi_a)^2} \right)$	10^{-11}	2.86×10^{-11}
	10^{-9}	2.86×10^{-9}
	10^{-7}	3.45×10^{-7}
$\frac{M_a}{2M_0} \left((\psi + \kappa) \frac{\psi_0}{\psi_a} \right)^{-1/2}$	10^{-11}	1.98×10^{-11}
	10^{-9}	1.99×10^{-9}
	10^{-7}	2.27×10^{-7}
$\frac{M_a}{20M_0} \frac{\psi_0}{\psi_a} \left((\psi + \kappa) \frac{\psi_0}{\psi_a} \right)^{-1}$	10^{-11}	2.82×10^{-12}
	10^{-9}	2.82×10^{-10}
	10^{-7}	4.10×10^{-8}

IX. CONCLUSIONS

Previous research on the process of magnetic burial and accreting neutron stars has resorted to analytically guessing the form of $F(\psi)$ and $dM/d\psi$. This research provides insight on how sensitive the functional form of the mass-flux is to alterations. Altering the $dM/d\psi$ three times and plotting the contour plots of the magnetohydrodynamic properties of the star after accretion, has shown noticeable differences in results. Thus, implying that there is some level of dependence on the form of the mass-flux function.

Nevertheless, the errors found in some of the contour plots need further analysis to ensure that our results are accurate. Majority of the differences between the reproduction of plots from [1] are due to machine precision error or rounding errors, so we assume that the lowest value contours (purple) are consistent with being zero. However, plots of ∇P have significant instabilities.

Additionally, to further improve this research the code can be altered to include analysis beneath the surface of the star. A three-dimensional model of magnetic burial for neutron stars in x-ray binary systems could also provide interesting results to further this field similar to methods by a recent publication [3]. Also, a more realistic equations of state could provide more interesting results. An adiabatic atmosphere rather than isothermal has been altered from previous research in the GS code and is yet to be utilized with these new results.

Finally, the recent search for continuous gravitational waves in [7] alongside the research described in this paper suggests the plausibility of detections in the near future. Conversely, the non-detection to this point marginally constrains the physics of magnetically confined mountains which could provide even more insight on the mysteries of magnetic fields and their origins.

Acknowledgments

This research would not have been possible without the guidance of Melatos and Brunet I would like to thank my mentor Melatos for all his guidance on this project, as well as his PhD student Brunet, who met with me every week, provided me with resources, and answered all my questions throughout this research. Thank you to Dr. Jonathan Zrake for his feedback and expertise in this area after proof reading this paper. Additionally, thank you to Peter Fulda, Paul Wass, and everyone from University of Florida who made this IREU possible during these uncertain times. Finally, I would like to thank the National Science Foundation for funding this research. NSF Funding: NSF PHY-1950830 and NSF PHY-1460803.

Appendix

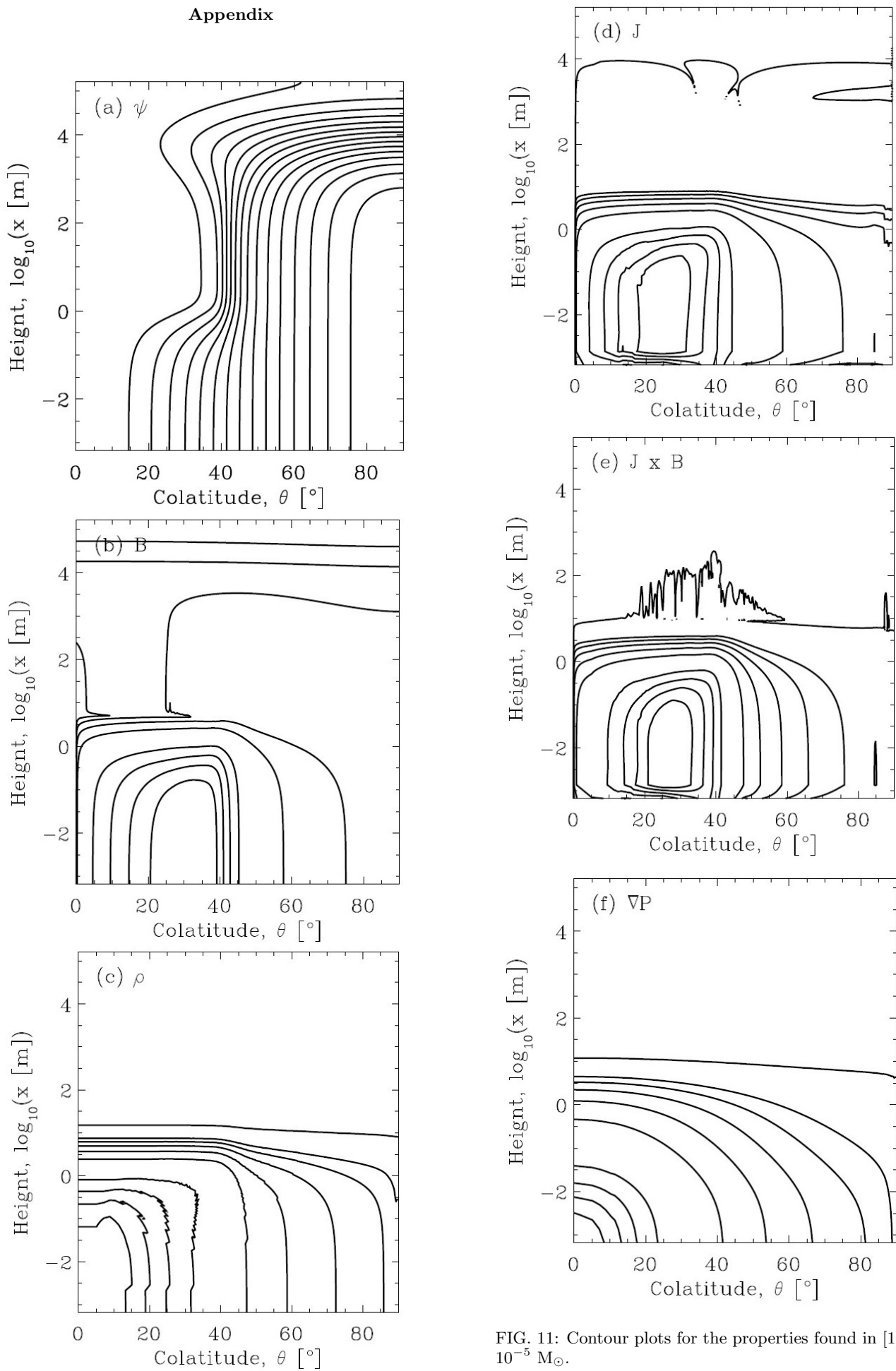


FIG. 11: Contour plots for the properties found in [1]. $M_a = 10^{-5} M_\odot$.

-
- [1] Melatos, A., Payne, D. J. B., 2004, *Mon. Not. R. Astron. Soc.* 351, 569–584.
- [2] Haskell, B., Priyamak, M., Patruno, A., Oppenoorth, M., Melatos, A., Lasky, P. D., 2015, *Mon. Not. R. Astron. Soc.* arXiv:1501.06039.
- [3] Sur, A., Haskell, B., 2021, PASA, doi: 10.1017/pas.2021.xxx.
- [4] Bhattacharya, D., 2002, *J. Astrophys. Astr.* 23, 67–72.
- [5] Melatos, A., Phinney, E. S., 2001, *Astron. Soc. Aust.*, 18, 421–430.
- [6] Priyamak, M., Melatos, A., Payne, D. J. B., 2011, *Mon. Not. R. Astron. Soc.* 417, 2696–2713.
- [7] LIGO Scientific Collaboration, Virgo Collaboration, KAGRA Collaboration, 2021, arXiv:2107.00600.